Overlimiting Ion Transport Dynamic toward Sand's Time in Solid Polymer Electrolytes

Youngju Lee^a, Bingyuan Ma^a, and Peng Bai^{a,b,*}

^a Department of Energy, Environmental and Chemical Engineering, Washington University in St. Louis, 1 Brooking Dr, St. Louis, MO 63130, USA.

^b Institute of Materials Science and Engineering, Washington University in St. Louis, 1 Brooking Dr, St. Louis, MO 63130, USA.

*Correspondence to: pbai@wustl.edu

Abstract

The ion transport dynamics in solid polymer electrolytes can be well captured by the classic Nernst-Planck equation under the dilute solution assumption. However, investigations on the characteristic Sand's time under various overlimiting currents are quite limited, partly due to the difficulties of determining the true current density and the accurate starting time of dendritic growths. Here, transparent microcapillary cells are fabricated to overcome these challenges. Our specialty cells not only minimize the possible discrepancy between the geometric current density and the true local current density by reducing the cross-sectional area, but also allow reliable determination of the Sand's time via direct *operando* optical observation. Sand's time simulations using both the dilute solution theory and the concentrated solution theory, with the parameters cross-validated by independent measurements, match closely with the experimental Sand's time. Our work demonstrates that the onset of lithium dendritic growths in solid polymer electrolytes may not always yield the familiar Sand's time voltage spike. Avoiding the localized overlimiting current density is the key to developing penetration-free polymer electrolytes.

Keywords: Solid polymer electrolytes, Li metal dendrites, Dilute solution theory, Concentrated solution theory, Sand's time

1 Introduction

The development of portable electronic devices and electric vehicles has been demanding more efficient and safer energy storage devices [1]. The utilization of Li metal as an anode brought lots of attention since it allows significantly higher energy and power densities compared to conventional graphite anodes [2,3]. However, the commercialization has been hindered by the dendrite formation, which leads to fast degradation and failure of the cells [2,4]. One route to prevent dendrite growth is to exploit ceramic or solid polymer electrolytes [5–7]. which can provide an extra mechanical driving force to stabilize the linear instabilities at the solid-solid interface [8]. However, two important assumptions of this seminal work, i.e. below the system-specific limiting current and without considering the localization of flux, have been overlooked by many investigations, which are critically important for understanding the observed localized lithium metal penetrations [9,10].

It has been demonstrated that classic Nernst-Planck equations, under the assumption of dilute solution theory, can be used to model the ion transport dynamics in solid polymer electrolytes [11–13]. Accordingly, lithium dendrite initiation should only occur when the applied current density is higher than the system-specific limiting current density, yet at the characteristic time when the concentration is depleted to zero at the electrode surface, i.e. at Sand's time [4,10,14]. Recently, Balsara et al. [15] demonstrated that both the rigorous concentrated solution theory [16–18] and the dilute solution theory predict similar limiting current densities [15] that agree very well with the experimental results. However, Sand's time formula based on the dilute solution theory [19], as another important equation that can confirm the transport dynamics, has not been tested systematically in solid polymer electrolytes. As demonstrated in our previous reports [4,10] not

only could Sand's time experiments verify the limiting current density, the scaling exponent between Sand's time and the overlimiting current densities could be used to infer the penetration structure through the electrolyte [10].

Rosso et al. [13] and several later studies [7,20–25], demonstrated the power-law scaling between Sand's time and current density, but there remain unanswered questions. The theoretical scaling exponent of -2 was indeed reported [7,13,21–23], but in many cases, the absolute values of Sand's times were an order of magnitude higher than the theoretical expectations [22,23]. Meanwhile, like what has been discovered in the liquid electrolytes with separators and fillers [26– 29], positively deviated scaling exponents (i.e. toward -1) were found in polymer electrolytes [20,25,30]. Still, dendritic growths were also observed at underlimiting current densities [13], where interfacial instabilities due to diffusion limitation should not occur. Most recently, Stolz et al. [7] investigated the Sand's time behaviors in Poly(ethylene oxide)-Lithium bis(trifluoromethanesulfonyl)imide (PEO-LiTFSI) electrolytes. By substituting an estimation of diffusion length at Sand's time, they proposed a "threshold current density" as a design criterion. While this threshold current density, smaller than the limiting current density by a factor of ~4, may suggest that the dendrite initiation could occur at underlimiting current densities, rigorous comparison with the system-specific limiting current density is needed, for which the discrepancy between the apparent current density and the true local current density must be minimized [10,13].

Here, we investigate the polarization process inside solid polymer electrolytes by examining optical *operando* experiments using special capillary cells that ideally match the classic one-dimensional transport model. Our work focuses on obtaining, via direct experiments, the Sand's time, limiting current density, ionic conductivity, and the transference number of Li-ions, to

achieve a comprehensive yet self-consistent understanding of the dendrite initiation and penetration dynamics in solid polymer electrolytes.

2 Results

2.1 Ionic conductivity at various temperatures

Transparent glass capillary cells [4,10] for *operando* observation were filled with PEO-LiTFSI solid electrolyte and two pieces of lithium metals to form a lithium|PEO-LiTFSI|Lithium symmetric cell. Using these capillary cells, we first measured the ionic conductivity by electrochemical impedance spectroscopy (EIS) at 6 different temperatures from 30 to 100 °C. (Fig. 1a-b and Supplementary information, Fig. S1) The obtained Nyquist plots were fitted to the equivalent circuit model shown in Fig 1b to extract the bulk resistance, while the capacitance was calculated from the characteristic frequencies at the apex of the semicircles. (Supplementary information, Fig. S1) Both the bulk and interface resistances decrease as temperature increases, while the capacitance remained relatively constant (Figure S2). The conductivities converted from the bulk resistances were plotted in an Arrhenius plot (Fig. 1c). The conductivities were very close to the reported values for a similar polymer blend [6]. The activation energy calculated from the slope is 0.52 eV for the higher temperature range and 1.25 eV for the lower temperature range. The transition occurred around the melting temperature, beyond which the higher polymer chain mobility enabled higher conductivity [6].

Fig. 1. (a) The measured EIS spectra of the glass capillary cells filled with PEO-LiTFSI polymer electrolytes at different temperatures. Inset is the digital photo of the cell used in

the experiment. (b) Magnification of panel (a). Inset is the equivalent circuit model [6] used in the impedance analysis. (c) Arrhenius plot with the conductivity values calculated from bulk resistance. (d) Li-ion transference number in 15:1 PEO-LiTFSI electrolytes measured with the Bruce-Vincent method, compared with the values from the literature [18,31–33].

2.2 Transference number of Li⁺

The transference number of Li^+ (t_{Li}) is another important kinetic parameter for SPE systems [33]. Here, we adopt the method pioneered by Bruce and Vincent to determine t_{Li} for the PEO-LiTFSI chemistry but at the 6 different temperatures [18,31–33] (Fig. 1d). According to Bruce and Vincent, only the cation conductivity is responsible for the conductivity of the cell in the steady-state, and a resistance of the passivation film at the interface must be corrected out from the applied voltage [12,33]. The analysis leads to,

$$t_{Li} = \frac{I_{SS}(V - I_0 R_0)}{I_0(V - I_{SS} R_{SS})} \tag{1}$$

where I_0 denotes the initial transient current when the DC polarization is applied, I_{SS} the steady-state current during DC polarization, V the applied DC voltage, R_0 the initial interfacial resistance, R_{SS} the steady-state interfacial resistance.

In practice, only a small DC voltage was applied and EIS is utilized to measure the conductivity and film resistance. It is worth mentioning that for samples at high temperatures (80 and 100 °C), the amplitude of the DC voltage and EIS excitation was chosen at 10 mV. For samples at lower temperatures (30 \sim 70 °C), we had to increase the DC voltage and amplitude to 100 mV to obtain

stable impedance data. EIS excitations of 80 mV have been implemented to generate reliable impedance data in the literature [18]. For all temperatures, t_{Li} values reside in the range of 0.1~0.2 without clear temperature dependence (Fig. 1d), which is consistent with the report of Pozyczka et al. [33]. A transference number of 0.15 was used for our later simulations using both the dilute and concentrated solution theories unless mentioned otherwise. It's worth noting that Newman and coworkers proposed a compensated transference number ($t_{+,Ne}$) for the concentrated solution model [17,18,34], and even negative values of $t_{+,Ne}$ were reported, which was attributed to the presence of charged clusters such as [Li(TFSI)₂]⁻ [18,35]. This compensated transference number would reflect more physical meanings, but we used the traditional concept of transference number for the comparison with the dilute solution model.

2.3 System-specific limiting current density

To observe the Sand's time, overlimiting current densities must be applied. The system-specific limiting current densities were measured by chronoamperometry experiments at 5 V. The stabilized transient current density was taken as the limiting current density (Supplementary information, Fig. S3a).

The experimental limiting current density can be used to determine the diffusion coefficient of the salt, via either the dilute solution theory or the concentrated solution theory [16]. For the concentrated solution model, COMSOL Multiphysics software was utilized for the numerical calculations. (Supplementary information Eq. S1-S5) Interestingly, both theories predicted virtually the same limiting current density when the same system constants and diffusion coefficient were adopted (Fig. 2a). In a recent study of PEO-LiTFSI systems with different EO-

to-Li ratios, predictions of the limiting current densities using these two theories were also very close [15]. However, care must be taken in discussing the diffusion processes, although the subtle differences between the definitions of the "many" diffusion coefficients are easily overlooked.

In the concentrated solution theory, the diffusion coefficient of the salt (D) is defined as

$$D = \mathcal{D}\frac{c_T}{c_0} \left(1 + \frac{\partial \ln \gamma}{\partial \ln m}\right) \tag{2}$$

where the cursive \mathcal{D} is the diffusion coefficient of the *electrolyte* (salt and solvent) under the thermodynamic driving force. c_T is the total concentration including that of the solvent, c_0 the solvent concentration, γ the mean molal activity coefficient of the salt, and m the molality of the electrolyte [16]. The diffusion coefficient in the dilute solution theory, however, is the ambipolar diffusion coefficient (D_{amb}) defined as,

$$D_{amb} = \frac{z_{+}u_{+}D_{-} - z_{-}u_{-}D_{+}}{z_{+}u_{+} - z_{-}u_{-}}$$
(3)

where z_i denotes the charge number, D_i the diffusion coefficient, and u_i the mobility of the individual species i [36], i.e. either the cation (+) or the anion (-).

Neither the D in Eq (2) nor the $D_{\rm amb}$ in Eq (3) denotes the diffusion coefficient of Li ions. They are the effective diffusion coefficients reflecting the collective behavior of diffusion and migration with contributions from both the cations and the anions, and with thermodynamic corrections. In practice, the *measured* diffusion coefficient via electrochemical methods should be interpreted as either D in the concentrated solution theory or $D_{\rm amb}$ in the dilute solution theory, which will lead

to a slightly different explanation of the fundamental physics, especially the potential distribution in the electrolyte as we shall discuss later [16]. PFG NMR (pulse-field gradient nuclear magnetic resonance) has been used to detect the diffusion coefficient of Li ions [37]. This *tracer* diffusion coefficient should be regarded as D_+ in Eq (3), but not the D_{amb} , because the latter contains the effect of migration and the contribution from the anions [16]. It is then necessary to stress that, according to the dilute solution theory, the transference number of cations for the binary electrolyte is defined as:

$$t_{+} = 1 - t_{-} = \frac{z_{+}u_{+}}{z_{+}u_{+} - z_{-}u_{-}} \tag{4}$$

With this expression, equation (3), and Einstein relation ($D_i = RTu_i$), one can obtain the mathematical identity $D_{amb} = 2t-D_+$, with which the limiting current density (J_{lim}) derived from the dilute solution theory can be expressed in two equivalent ways:

$$J_{lim} = \frac{2Z_{+}C_{0}FD_{amb}}{t_{-}L} = \frac{4Z_{c}C_{0}FD_{+}}{L}$$
(5)

where Z_+ denotes the charge number of cation, C_0 the bulk salt concentration (not to be confused with the lower-case c_0 for solvent concentration), F the Faraday's constant, D_{amb} the ambipolar diffusion coefficient, D_+ the Li-ion diffusion coefficient, t_- the transference number of anion, and L the distance between two electrodes. The second identity in Equation (5) tells that the transference number is a secondary/derived parameter, which is not necessary whenever the diffusion coefficient of Li^+ can be precisely obtained, unless the dilute solution theory is no longer valid for the specific case. Nevertheless, the Sand's time (t_8) equation still explicitly contains the

transference number, which cannot be eliminated by the known mathematical identities listed above:

$$t_S = \frac{\pi D_{amb} (Z_+ C_0 F)^2}{4(Jt_-)^2} = \frac{\pi D_+ (Z_+ C_0 F)^2}{2t_- J^2}$$
(6)

where J is the overlimiting current density ($J > J_{\text{lim}}$) that drives the complete concentration depletion at the electrode surface. To determine D_{amb} or D_{+} from Sand's time, an independently pre-determined t_{-} or t_{+} is required.

Fig. 2. (a) Limiting current densities for different temperatures, calculated from the current plateaus in chronoamperometry curves. Simulation results from both the dilute and concentrated solution theory are also included. (b) Calculated Li-ion diffusivities from limiting current density and conductivity, compared with literature data [7,37,38]. Number n represents the EO to Li ratio, which is 15 for this work.

Here, we compared the diffusion coefficients of Li ions, i.e. D_+ , calculated from the experimental limiting current density (Eq. 5), from the conductivity using the procedures outlined in the Supplementary information (Eq. S7), and from the experimental Sand's time (Eq. 6), which are all plotted in Fig. 2b. The diffusion coefficient derived from ionic conductivity (D_σ) through the Nernst-Einstein relation can be related to the tracer diffusion coefficient of Li ions ($D^*=D_+$) via the Haven ratio ($H_R = D^*/D_\sigma$). For the values presented in Fig. 2b, we assumed $H_R = 1$, although other values < 1 should be used if there exists a strong correlation between different ion species or between ion and skeleton [39]. The literature data of Li-ion diffusion coefficient in PEO-LiTFSI systems are also included, with annotations of the corresponding measurement techniques

[7,33,37,38,40,41]. Despite that the EO-to-Li ratio of our SPE is not identical to all the other cases, the values and trend of the diffusion coefficients match closely with the literature data.

2.4 Determination of Sand's time via operando visualization

Existing studies rely on the voltage spike in the chronopotentiometry experiments to determine whether the current was an overlimiting current [15], or the Sand's time [7]. Here, we utilized the *operando* glass capillary cells filled with PEO-LiTFSI electrolyte to directly determine the dendrite initiation at various temperatures and then compare the measured Sand's time with the theoretical predictions by both the dilute solution and the concentrated solution theories.

Fig. 3. Representative voltage curves and corresponding *operando* images of the glass capillary cells during galvanostatic charging. (a-e) 30 °C, current density of 0.03 mA / cm². (f-j) 50 °C, current density of 0.15 mA / cm². (k-o) 60 °C, 0.4 mA / cm². The points labeled by the red arrowheads mark the Sand's time.

The determination of the Sand's time for the SPE system, unlike the liquid systems, was challenging due to multiple factors, such as the mechanical stabilization and the heterogeneous nature of the polymer matrix. However, our *operando* images greatly increase the reliability of interpreting the characteristic points found in the voltage curves. The representative curves and key *operando* images obtained at different temperatures are shown in Figs. 3 and 4. Additional voltage curves and *operando* images associated with the Sand's time data points presented in this work can be found in the supplementary information. (Fig. S4-S19).

For the sample tested at 30 °C, a clear dendrite tip was observed at the time point (d), indicated by the red arrowheads in Figs. 3a and 3d, where the expected voltage pike emerged only after nearly 15,000 seconds at the time point (e), where many dendrite tips had already been induced (Fig. 3e). This time delay between the actual dendrite initiation and the voltage spike due to complete concentration depletion occurs in low-temperature cases and is attributable to the rigid yet heterogeneous nature of the SPE, in which certain spots at the interface attracted a focused flux and then experienced stronger depletion. For the sample tested at 50 °C, no voltage spike was observed during the chronopotentiometry experiments, even though overlimiting current densities were applied, and dendritic growths were observed. Our results demonstrate the necessity of operando techniques, as even some modest operando techniques can improve the traditional method that only relies on the voltage spike to understand the ion depletion and dendrite initiation dynamics. The phenomenon that dendrites initiated near a finite voltage hump, rather than at a diverging voltage spike, followed by a noisy current plateau found in our SPE cells at 30 °C and 50 °C was also encountered in liquid electrolytes [4,10]. It is probable that the growth speed of a local dendrite in the depleted region may leap-frog the retreating concentration front to receive an ample supply of ions, yielding a finite noisy current plateau. Cheng et al. recently reported that ion depletion can induce phase transformation of the polymer with a significantly increased modulus [42], leading to further stabilization of Li deposition.

For the samples tested at 60 °C (Fig. 3k), 70 °C (Fig. 4a), and 80 °C (Fig. 4f), the time of dendrite emergence is consistent with the time when a clear slope change in the voltage curve is observed. In some of the tests, the voltage responses resemble that of the 50 °C cases, where only a finite voltage hump was observed and followed by a noisy plateau (Supplementary information, Fig. S6).

For the 100 °C cases (Fig. 4k) and a number of our 60 °C samples (Supplementary information Fig. S9), a very sharp potential peak was observed, and the cell got shut down shortly after, without any visible dendrites. Note that such behavior was also discovered in liquid electrolyte cases, such as electrolytes with triglyme [10]. A comparison of the initial and final states reveals that there is indeed visible Li deposition before the voltage spike at Sand's time, which appears to be a shiny surface growth (Supplementary video). Current densities lower than the system-specific limiting current density (1 mA cm⁻²) resulted in a very smooth, shining surface growth (Supplementary information, Fig. S20). Whether this ideal interfacial stability guarantees absolute safety [43,44] still requires further investigation at multiple underlimiting current densities.

Fig. 4. Representative voltage curves and corresponding *operando* images of the glass capillary cells during galvanostatic charging. (a-e) 70 °C, current density of 0.03 mA / cm². (f-j) 80 °C, current density of 0.15 mA / cm². (k-o) 100 °C, 1.2 mA / cm². The points labeled by the red arrowheads mark the Sand's time.

2.5 Theoretical predictions of Sand's time

The concentrated solution theory was previously adopted for simulating the SPE systems [16,45,46], but to the best of our knowledge, calculations of the Sand's time were never attempted. Using the diffusion coefficients determined earlier, the theoretical Sand's times from both the

dilute solution theory and the concentrated solution theory agree well with the experimental Sand's times obtained in various conditions (Fig. 5). For the Sand's time predicted by the concentrated solution theory, the COMSOL simulations were utilized to determine the time until the complete concentration depletion at the electrode surface. (Supplementary information, Fig. S21) All three data sets show a similar power-law correlation in each logarithmic plot. Only in the case of 50 °C, the actual values of the experimental Sand's times were significantly lower than the theoretical predictions. While the precision understanding requires further investigation, this is not unexpected, as it is consistent with the Arrhenius plot of the ionic conductivities (Fig 1c), in which the conductivity (i.e. the conduction mechanisms) had a sharp change at 50 °C. Note that experimentally measured Sand's time can be used to determine Sand's capacities at different temperatures as the maximum safe operation capacity, i.e. avoiding the concentration depletion and dendritic growths (Supplementary information Fig. S22). It must be pointed out that the safety boundaries for lower working temperatures are significantly lower due to the more sluggish transport kinetics.

Fig. 5. Logarithmic plot of measured Sand's time versus the current density, compared with predictions from dilute and concentrated solution theory. For the concentrated solution theory model, a value of 2 was used for the thermodynamic factor $(1 + \partial \ln \gamma / \partial \ln m)$. For 60 °C and 80 °C data, average values were presented with error bars which show standard deviations.

In the numerical simulation of Sand's time, D_{amb} in the dilute solution theory and D in the concentrated solution theory were set to be the same measured diffusion coefficients, consistent

with their respective definitions. The predicted Sand's times showed negligible differences (Fig. 6a). This, however, does not undermine the significance of the concentrated solution theory, as the thermodynamic factor $(1 + \partial \ln \gamma / \partial \ln m)$, which is part of the D, also plays an important role in the flux equation (Supplementary information, Eq. S4), determining the correct interpretation of the potential. The thermodynamic factor $1 + \partial \ln \gamma / \partial \ln m$, where γ is the mean molar activity coefficient of the salt and m is the molarity, is related to minor component interactions such as solvation and the nature of ion association [18,35]. As shown in Fig. 6b, we included three cases in our simulations. The thermodynamic factor $(1 + \partial \ln \gamma / \partial \ln m)$ of 1 corresponds to the dilute solution case where γ is 1, i.e. $\partial \ln \gamma / \partial \ln m = 0$. Based on the EO-to-Li ratio, we also included the case of $1 + \partial \ln \gamma / \partial \ln m = 2$, according to the recent literature reporting the concentration dependence of the thermodynamic factor [18]. A thermodynamic factor of 12 was also included here, as it was reported to be the case of a high-molecular-weight PEO, similar to our samples [47]. As can be seen in Fig. 6b, different thermodynamic factors resulted in vastly different cell potential, emphasizing the importance of salt and polymer chains interactions. The prediction with the thermodynamic factor value of 2 matched closely with our experimental data. Note that the COMSOL module for our simulation ended at the point of the complete ion depletion.

Fig. 6. (a) Sand's time and (b) example cell potential (100 °C, 1.8 mA / cm²), predicted by the concentration model with different thermodynamic factor $(1 + \partial \ln \gamma / \partial \ln m)$ values.

3 Discussions

To observe the Sand's time voltage spike, an overlimiting current density is required. While we emphasized that the limiting current density depends on the system constant, L, the distance between two electrodes, the characteristic Sand's time does not. This is because the overlimiting current density (i.e. $J > J_{\text{lim}}$) that can drive the complete concentration depletion to show the Sand's time voltage spike will always generate a diffusion layer thinner than, yet independent from L. Otherwise, any current densities small than the limiting current density will reach a steady state across the whole system, with a concentration gradient of $2C_0/L$, unless the current distribution at the two-dimensional electrode surface is highly nonuniform.

The above theoretical analysis and simulations assumed an open/homogeneous electrolyte to connect the two electrodes. However, in reality, the nonideal solid electrolyte or porous separator would interfere with the current distribution at the electrode surface. Metal deposits may preferentially grow into a local pore even at underlimiting current densities ($J < J_{lim}$) [43], which will lead to strong localization of the incoming ionic flux to yield a local overlimiting current density and trigger the fast dendritic growth through a self-guided yet isolated path [10]. According to the simulation done by Barai et al. [48,49] which considered the mechanical properties of the polymer, only 40 % of the limiting current density was enough to form dendrites. The heterogeneous local ionic concentration and the effect on dendrite growth were also reported by Cheng et al. [50] who utilized operando stimulated Raman scattering microscopy. Rigorous analysis of the current distribution near the electrode surface, at current densities lower but close to the limiting current density, may facilitate the alleviation of such flux localization effect.

According to the more general structure-dependent Sand's time equation based on capillary cell experiments using liquid electrolytes [15], the nonideal scaling exponents (not equal to -2) may indicate the geometry of the ionic conduction path, or the structure of the metal penetration. Here, we discovered that the Sand's time scaling exponents for cells tested at 30 °C -80 °C all showed a positive deviation (slope >-2), and cells tested at 100 °C showed a negative deviation (slope =-2.50). However, unlike in liquid electrolytes, we were not able to observe significant growths of dendrites to infer the convergence of the penetration structure, due to the much slower growths in the PEO-LiTFSI electrolytes, even at 100 °C when the polymer behaviors like a liquid with sufficiently high conductivities.

4 Conclusion

Through the combined experimental and theoretical analyses, we have demonstrated that simple operando imaging of transparent glass capillary cells can greatly enhance the reliability of traditional electroanalytical techniques, by providing direct evidence of dendrite emergence, especially for the PEO-LiTFSI solid polymer electrolytes, where the electrochemical features are not always the same as those in the liquid electrolytes. By performing independent measurements to get the transference number, ionic conductivity, limiting current density, and Sand's time, we were able to cross-validate the diffusion coefficients, with an emphasis on the differences of the different diffusion coefficients defined in different theories and methods. Our simulation results further demonstrated that both the dilute solution theory and the concentrated solution theory predicted similar limiting current densities and similar Sand's times for all cases. However, the

concentrated solution theory is necessary to correctly interpret the corresponding cell potential. Our results suggested that rigorous analysis of the current distribution at current densities lower than but close to the system-specific limiting current density is critical for understanding the localized penetration, which will facilitate the development of safe metal batteries.

5 Material and methods

5.1 Preparation of glass capillary cells with SPE

Electrochemical cells with the 2-electrode configuration were fabricated with the glass capillaries with internal diameters of 300 um (VWR, 5 μL Micropipets). The polymer electrolyte samples were prepared by following the steps of the works by Sakamoto et al. [6]. Polyethylene Oxide (PEO, MW 4,000,000, poly sciences), LiTFSI (99.95 %, Sigma Aldrich), and acetonitrile (99.8 %, Sigma Aldrich) were used for the fabrication of PEO-LiTFSI electrolyte. The PEO and LiTFSI powders were vacuumed dried at 60 °C for 24 hours and mixed with acetonitrile to form a gel-like solution. The mixture was stirred for 24 hours at room temperature and then was stirred for 12 hours at 60 °C. The ratio of O/Li was controlled to be 15:1. The prepared mixture was injected into a glass capillary and then at room temperature with a partial vacuum applied (127 torrs) for 24 hours, and then it was vacuum dried at 60 °C. The dried glass capillary had a coating PEO-LiTFSI on the inner walls, which was scrubbed to form a full filling in the center part of the capillary. Both sides of the filling were sealed with Li metal pieces, and stainless-steel wires were used as the current collector.

5.2 Electrochemical testing in various temperatures

To perform electrochemical testing in various temperatures while capturing the *operando* microscopic images, we installed an infrared heat lamp to the optical microscope (MU500, AmScope). The power to the lamp was connected with a PID controller which was connected to a thermocouple temperature sensor. The sample preparation, cell assembly, and electrochemical experiments were done inside a glovebox filled with argon gas with water and oxygen concentration less than 0.5 ppm. Galvanostatic charge testing and EIS spectra measurement were done with a Gamry potentiostat (Reference 600+, Gamry Instruments).

Acknowledgments

This work is supported by a National Science Foundation grant (Award No. 1934122). P.B. acknowledges the startup support from Washington University in St. Louis.

Data availability

The raw/processed data required to reproduce these findings cannot be shared at this time due to technical or time limitations.

References

- [1] J.-M. Tarascon, M. Armand, Issues and challenges facing rechargeable lithium batteries, Nature. 414 (2001) 359–367. https://doi.org/10.1038/35104644.
- [2] W. Xu, J. Wang, F. Ding, X. Chen, E. Nasybulin, Y. Zhang, J.G. Zhang, Lithium metal anodes for rechargeable batteries, Energy Environ. Sci. 7 (2014) 513–537. https://doi.org/10.1039/c3ee40795k.
- [3] Z. Li, J. Huang, B. Yann Liaw, V. Metzler, J. Zhang, A review of lithium deposition in lithium-ion and lithium metal secondary batteries, J. Power Sources. 254 (2014) 168–182. https://doi.org/10.1016/j.jpowsour.2013.12.099.
- [4] P. Bai, J. Li, F.R. Brushett, M.Z. Bazant, Transition of lithium growth mechanisms in liquid electrolytes, Energy Environ. Sci. 9 (2016) 3221–3229. https://doi.org/10.1039/C6EE01674J.

- [5] X.B. Cheng, C.Z. Zhao, Y.X. Yao, H. Liu, Q. Zhang, Recent Advances in Energy Chemistry between Solid-State Electrolyte and Safe Lithium-Metal Anodes, Chem. 5 (2019) 74–96. https://doi.org/10.1016/j.chempr.2018.12.002.
- [6] A. Gupta, E. Kazyak, N. Craig, J. Christensen, N.P. Dasgupta, J. Sakamoto, Evaluating the Effects of Temperature and Pressure on Li/PEO-LiTFSI Interfacial Stability and Kinetics, J. Electrochem. Soc. 165 (2018) A2801–A2806. https://doi.org/10.1149/2.0901811jes.
- [7] L. Stolz, G. Homann, M. Winter, J. Kasnatscheew, The Sand equation and its enormous practical relevance for solid-state lithium metal batteries, Mater. Today. 44 (2021) 9–14. https://doi.org/10.1016/j.mattod.2020.11.025.
- [8] C. Monroe, J. Newman, The Impact of Elastic Deformation on Deposition Kinetics at Lithium/Polymer Interfaces, J. Electrochem. Soc. 152 (2005) A396. https://doi.org/10.1149/1.1850854.
- [9] K.J. Harry, D.T. Hallinan, D.Y. Parkinson, A.A. MacDowell, N.P. Balsara, Detection of subsurface structures underneath dendrites formed on cycled lithium metal electrodes, Nat. Mater. 13 (2014) 69–73. https://doi.org/10.1038/nmat3793.
- [10] Y. Lee, B. Ma, P. Bai, Concentration polarization and metal dendrite initiation in isolated electrolyte microchannels, Energy Environ. Sci. 13 (2020) 3504–3513. https://doi.org/10.1039/d0ee01874k.
- [11] C. Monroe, J. Newman, Dendrite Growth in Lithium/Polymer Systems, J. Electrochem. Soc. 150 (2003) A1377. https://doi.org/10.1149/1.1606686.

- [12] P.G. Bruce, C.A. Vincent, Steady state current flow in solid binary electrolyte cells, J. Electroanal. Chem. Interfacial Electrochem. 225 (1987) 1–17. https://doi.org/10.1016/0022-0728(87)80001-3.
- [13] M. Rosso, T. Gobron, C. Brissot, J.N. Chazalviel, S. Lascaud, Onset of dendritic growth in lithium/polymer cells, J. Power Sources. 97–98 (2001) 804–806. https://doi.org/10.1016/S0378-7753(01)00734-0.
- [14] J.N. Chazalviel, Electrochemical aspects of the generation of ramified metallic electrodeposits, Phys. Rev. A. 42 (1990) 7355–7367.
 https://doi.org/10.1103/PhysRevA.42.7355.
- [15] D.A. Gribble, L. Frenck, D.B. Shah, J.A. Maslyn, W.S. Loo, K.I.S. Mongcopa, D.M. Pesko, N.P. Balsara, Comparing Experimental Measurements of Limiting Current in Polymer Electrolytes with Theoretical Predictions, J. Electrochem. Soc. 166 (2019) A3228–A3234. https://doi.org/10.1149/2.0391914jes.
- [16] J. Newman, K.E. Thomas-Alyea, Electrochemical systems. Third edition, 2004. https://doi.org/10.1192/bjp.112.483.211-a.
- [17] N.P. Balsara, J. Newman, Relationship between Steady-State Current in Symmetric Cells and Transference Number of Electrolytes Comprising Univalent and Multivalent Ions, J. Electrochem. Soc. 162 (2015) A2720–A2722. https://doi.org/10.1149/2.0651514jes.
- [18] D.M. Pesko, K. Timachova, R. Bhattacharya, M.C. Smith, I. Villaluenga, J. Newman, N.P. Balsara, Negative Transference Numbers in Poly(ethylene oxide)-Based Electrolytes, J. Electrochem. Soc. 164 (2017) E3569–E3575. https://doi.org/10.1149/2.0581711jes.

- [19] H.J.S. Sand, III. On the concentration at the electrodes in a solution, with special reference to the liberation of hydrogen by electrolysis of a mixture of copper sulphate and sulphuric acid, London, Edinburgh, Dublin Philos. Mag. J. Sci. 1 (1901) 45–79. https://doi.org/10.1080/14786440109462590.
- [20] S. Liu, N. Imanishi, T. Zhang, A. Hirano, Y. Takeda, O. Yamamoto, J. Yang, Effect of nano-silica filler in polymer electrolyte on Li dendrite formation in Li/poly(ethylene oxide)-Li(CF3SO2)2N/Li, J. Power Sources. 195 (2010) 6847–6853. https://doi.org/10.1016/j.jpowsour.2010.04.027.
- [21] L. Sannier, R. Bouchet, M. Rosso, J.M. Tarascon, Evaluation of GPE performances in lithium metal battery technology by means of simple polarization tests, J. Power Sources. 158 (2006) 564–570. https://doi.org/10.1016/j.jpowsour.2005.09.026.
- [22] R. Khurana, J.L. Schaefer, L.A. Archer, G.W. Coates, Suppression of lithium dendrite growth using cross-linked polyethylene/poly(ethylene oxide) electrolytes: A new approach for practical lithium-metal polymer batteries, J. Am. Chem. Soc. 136 (2014) 7395–7402. https://doi.org/10.1021/ja502133j.
- [23] Z. Huang, Q. Pan, D.M. Smith, C.Y. Li, Plasticized Hybrid Network Solid Polymer Electrolytes for Lithium-Metal Batteries, Adv. Mater. Interfaces. 6 (2019) 1–8. https://doi.org/10.1002/admi.201801445.
- [24] S. Choudhury, R. Mangal, A. Agrawal, L.A. Archer, A highly reversible room-temperature lithium metal battery based on crosslinked hairy nanoparticles, Nat. Commun. 6 (2015) 1–9. https://doi.org/10.1038/ncomms10101.

- [25] S. Liu, N. Imanishi, T. Zhang, A. Hirano, Y. Takeda, O. Yamamoto, J. Yang, Lithium Dendrite Formation in Li/Poly(ethylene oxide)—Lithium Bis(trifluoromethanesulfonyl)imide and N-Methyl-N-propylpiperidinium Bis(trifluoromethanesulfonyl)imide/Li Cells, J. Electrochem. Soc. 157 (2010) A1092. https://doi.org/10.1149/1.3473790.
- [26] Y. Lu, K. Korf, Y. Kambe, Z. Tu, L.A. Archer, Ionic-liquid-nanoparticle hybrid electrolytes: Applications in lithium metal batteries, Angew. Chemie Int. Ed. 53 (2014) 488–492. https://doi.org/10.1002/anie.201307137.
- [27] Y. Lu, S.K. Das, S.S. Moganty, L.A. Archer, Ionic liquid-nanoparticle hybrid electrolytes and their application in secondary lithium-metal batteries, Adv. Mater. 24 (2012) 4430–4435. https://doi.org/10.1002/adma.201201953.
- [28] Y. Lu, Z. Tu, J. Shu, L.A. Archer, Stable lithium electrodeposition in salt-reinforced electrolytes, J. Power Sources. 279 (2015) 413–418. https://doi.org/10.1016/j.jpowsour.2015.01.030.
- [29] Y. Lu, Z. Tu, L.A. Archer, Stable lithium electrodeposition in liquid and nanoporous solid electrolytes, Nat. Mater. 13 (2014) 961–969. https://doi.org/10.1038/nmat4041.
- [30] C. Brissot, M. Rosso, J.-N. Chazalviel, S. Lascaud, Study of the evolution of the Li/electrolyte interface during cycling of Li/polymer batteries, in: Stud. Surf. Sci. Catal., 2001: pp. 947–952. https://doi.org/10.1016/S0167-2991(01)82243-6.

- [31] L. Edman, M.M. Doeff, A. Ferry, J. Kerr, L.C. De Jonghe, Transport Properties of the Solid Polymer Electrolyte System P(EO) n LiTFSI, J. Phys. Chem. B. 104 (2000) 3476–3480. https://doi.org/10.1021/jp993897z.
- [32] J. Mindemark, B. Sun, E. Törmä, D. Brandell, High-performance solid polymer electrolytes for lithium batteries operational at ambient temperature, J. Power Sources. 298 (2015) 166–170. https://doi.org/10.1016/j.jpowsour.2015.08.035.
- [33] K. Pożyczka, M. Marzantowicz, J.R. Dygas, F. Krok, IONIC CONDUCTIVITY AND LITHIUM TRANSFERENCE NUMBER OF POLY(ETHYLENE OXIDE):LiTFSI SYSTEM, Electrochim. Acta. 227 (2017) 127–135. https://doi.org/10.1016/j.electacta.2016.12.172.
- [34] M. Doyle, J. Newman, Analysis of Transference Number Measurements Based on the Potentiostatic Polarization of Solid Polymer Electrolytes, J. Electrochem. Soc. 142 (1995) 3465–3468. https://doi.org/10.1149/1.2050005.
- [35] I. Villaluenga, D.M. Pesko, K. Timachova, Z. Feng, J. Newman, V. Srinivasan, N.P. Balsara, Negative Stefan-Maxwell Diffusion Coefficients and Complete Electrochemical Transport Characterization of Homopolymer and Block Copolymer Electrolytes, J. Electrochem. Soc. 165 (2018) A2766–A2773. https://doi.org/10.1149/2.0641811jes.
- [36] J.-H. Han, E. Khoo, P. Bai, M.Z. Bazant, Over-limiting Current and Control of Dendritic Growth by Surface Conduction in Nanopores, Sci. Rep. 4 (2015) 7056. https://doi.org/10.1038/srep07056.

- [37] W. Gorecki, M. Jeannin, E. Belorizky, C. Roux, M. Armand, Physical properties of solid polymer electrolyte PEO(LiTFSI) complexes, J. Phys. Condens. Matter. 7 (1995) 6823–6832. https://doi.org/10.1088/0953-8984/7/34/007.
- [38] N.A. Stolwijk, M. Wiencierz, C. Heddier, J. Kösters, What can we learn from ionic conductivity measurements in polymer electrolytes? A case study on Poly(ethylene oxide) (PEO)-NaI and PEO-LiTFSI, J. Phys. Chem. B. 116 (2012) 3065–3074. https://doi.org/10.1021/jp2111956.
- [39] Y. Gao, A.M. Nolan, P. Du, Y. Wu, C. Yang, Q. Chen, Y. Mo, S.-H. Bo, Classical and Emerging Characterization Techniques for Investigation of Ion Transport Mechanisms in Crystalline Fast Ionic Conductors, Chem. Rev. 120 (2020) 5954–6008. https://doi.org/10.1021/acs.chemrev.9b00747.
- [40] D. Devaux, H. Leduc, P. Dumaz, M. Lecuyer, M. Deschamps, R. Bouchet, Effect of Electrode and Electrolyte Thicknesses on All-Solid-State Battery Performance Analyzed With the Sand Equation, Front. Energy Res. 7 (2020) 1–10. https://doi.org/10.3389/fenrg.2019.00168.
- [41] D.J. Brooks, B. V. Merinov, W.A. Goddard, B. Kozinsky, J. Mailoa, Atomistic Description of Ionic Diffusion in PEO–LiTFSI: Effect of Temperature, Molecular Weight, and Ionic Concentration, Macromolecules. 51 (2018) 8987–8995. https://doi.org/10.1021/acs.macromol.8b01753.
- [42] Q. Cheng, Y. Miao, Z. Liu, J. Borovilas, H. Zhang, S. Liu, H. Wang, X. Chen, L.-Q. Chen, W. Min, Y. Yang, Stabilizing lithium metal anode by ion depletion-induced phase

- transformation in polymer electrolytes, ChemRxiv. (2021) 1–17. https://doi.org/10.26434/chemrxiv.13726243.v1.
- [43] B. Ma, P. Bai, Fast Charging Limits of Ideally Stable Metal Anodes in Liquid Electrolytes, Adv. Energy Mater. (2022) 2102967. https://doi.org/10.1002/aenm.202102967.
- [44] B. Ma, Y. Lee, P. Bai, Dynamic Interfacial Stability Confirmed by Microscopic Optical Operando Experiments Enables High-Retention-Rate Anode-Free Na Metal Full Cells, Adv. Sci. 2005006 (2021) 1–11. https://doi.org/10.1002/advs.202005006.
- [45] J. Newman, D. Bennion, C.W. Tobias, Mass Transfer in Concentrated Binary Electrolytes, Berichte Der Bunsengesellschaft Für Phys. Chemie. 69 (1965) 608–612. https://doi.org/10.1002/bbpc.19650690712.
- [46] M. Doyle, T.F. Fuller, J. Newman, Modeling of Galvanostatic Charge and Discharge of the Lithium/Polymer/Insertion Cell, J. Electrochem. Soc. 140 (1993) 1526–1533. https://doi.org/10.1149/1.2221597.
- [47] P. Georén, G. Lindbergh, Characterisation and modelling of the transport properties in lithium battery polymer electrolytes, Electrochim. Acta. 47 (2001) 577–587. https://doi.org/10.1016/S0013-4686(01)00785-X.
- [48] P. Barai, K. Higa, V. Srinivasan, Effect of Initial State of Lithium on the Propensity for Dendrite Formation: A Theoretical Study, J. Electrochem. Soc. 164 (2017) A180–A189. https://doi.org/10.1149/2.0661702jes.

- [49] P. Barai, K. Higa, V. Srinivasan, Lithium dendrite growth mechanisms in polymer electrolytes and prevention strategies, Phys. Chem. Chem. Phys. 19 (2017) 20493–20505. https://doi.org/10.1039/c7cp03304d.
- [50] Q. Cheng, L. Wei, Z. Liu, N. Ni, Z. Sang, B. Zhu, W. Xu, M. Chen, Y. Miao, L.Q. Chen, W. Min, Y. Yang, Operando and three-dimensional visualization of anion depletion and lithium growth by stimulated Raman scattering microscopy, Nat. Commun. 9 (2018) 1–10. https://doi.org/10.1038/s41467-018-05289-z.

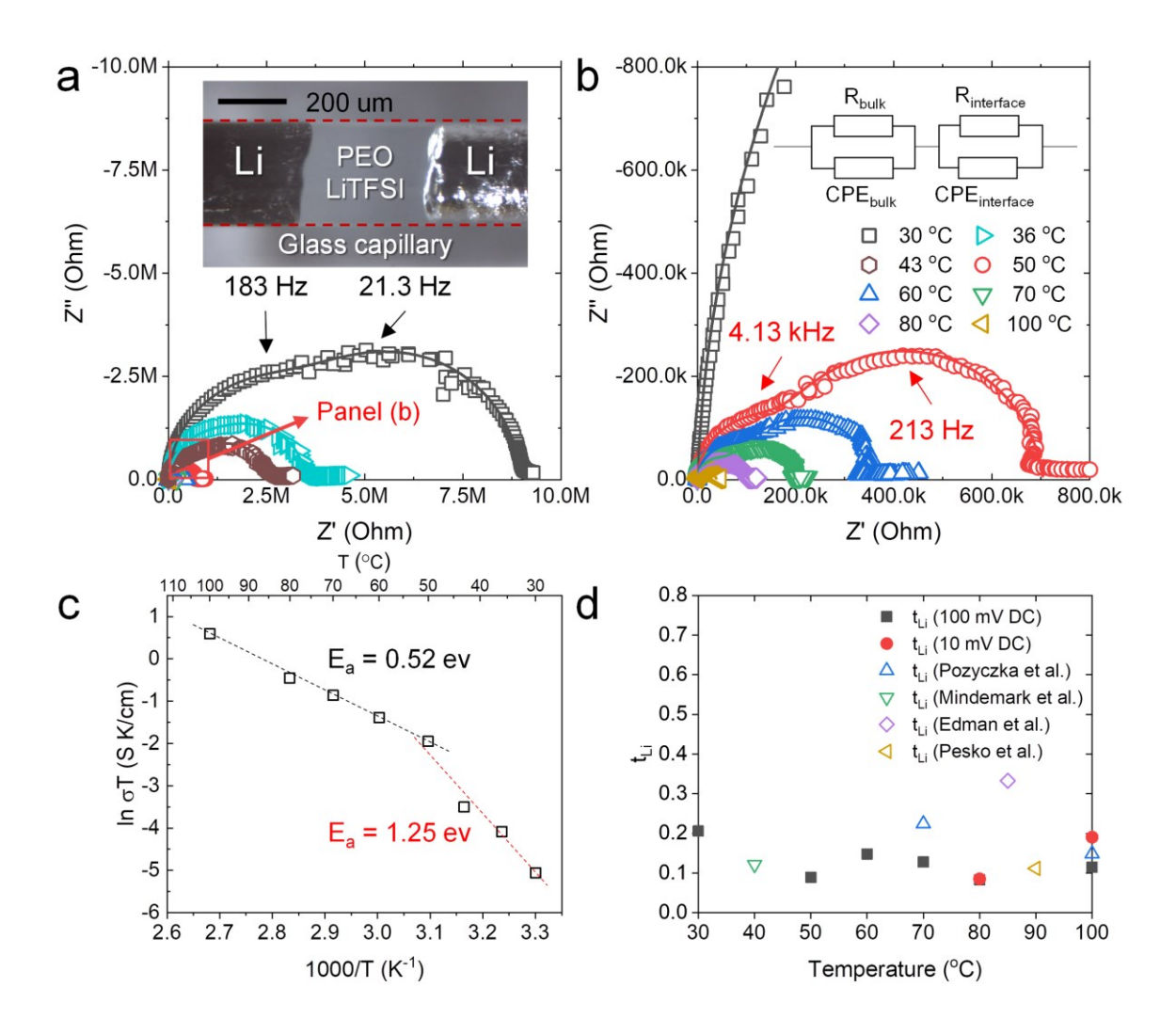


Fig. 1. (a) The measured EIS spectra of the glass capillary cells filled with PEO-LiTFSI polymer electrolytes at different temperatures. Inset is the digital photo of the cell used in the experiment. (b) Magnification of panel (a). Inset is the equivalent circuit model [6] used in the impedance analysis. (c) Arrhenius plot with the conductivity values calculated from bulk resistance. (d) Li-ion transference number in 15:1 PEO-LiTFSI electrolytes measured with the Bruce-Vincent method, compared with the values from the literature [18,31–33].

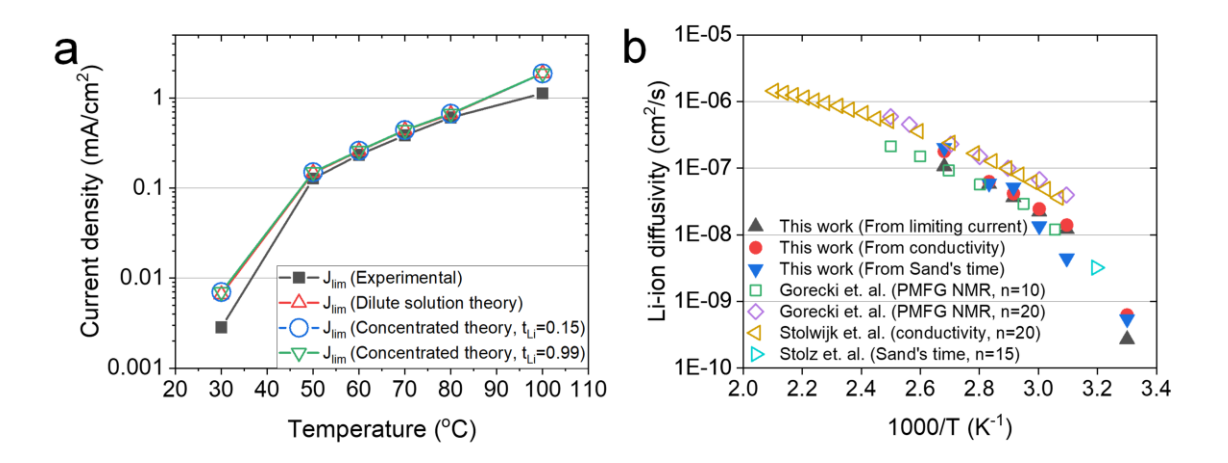


Fig. 2. (a) Limiting current densities for different temperatures, calculated from the current plateaus in chronoamperometry curves. Simulation results from both the dilute and concentrated solution theory are also included. (b) Calculated Li-ion diffusivities from limiting current density and conductivity, compared with literature data [7,37,38]. Number n represents the EO to Li ratio, which is 15 for this work.

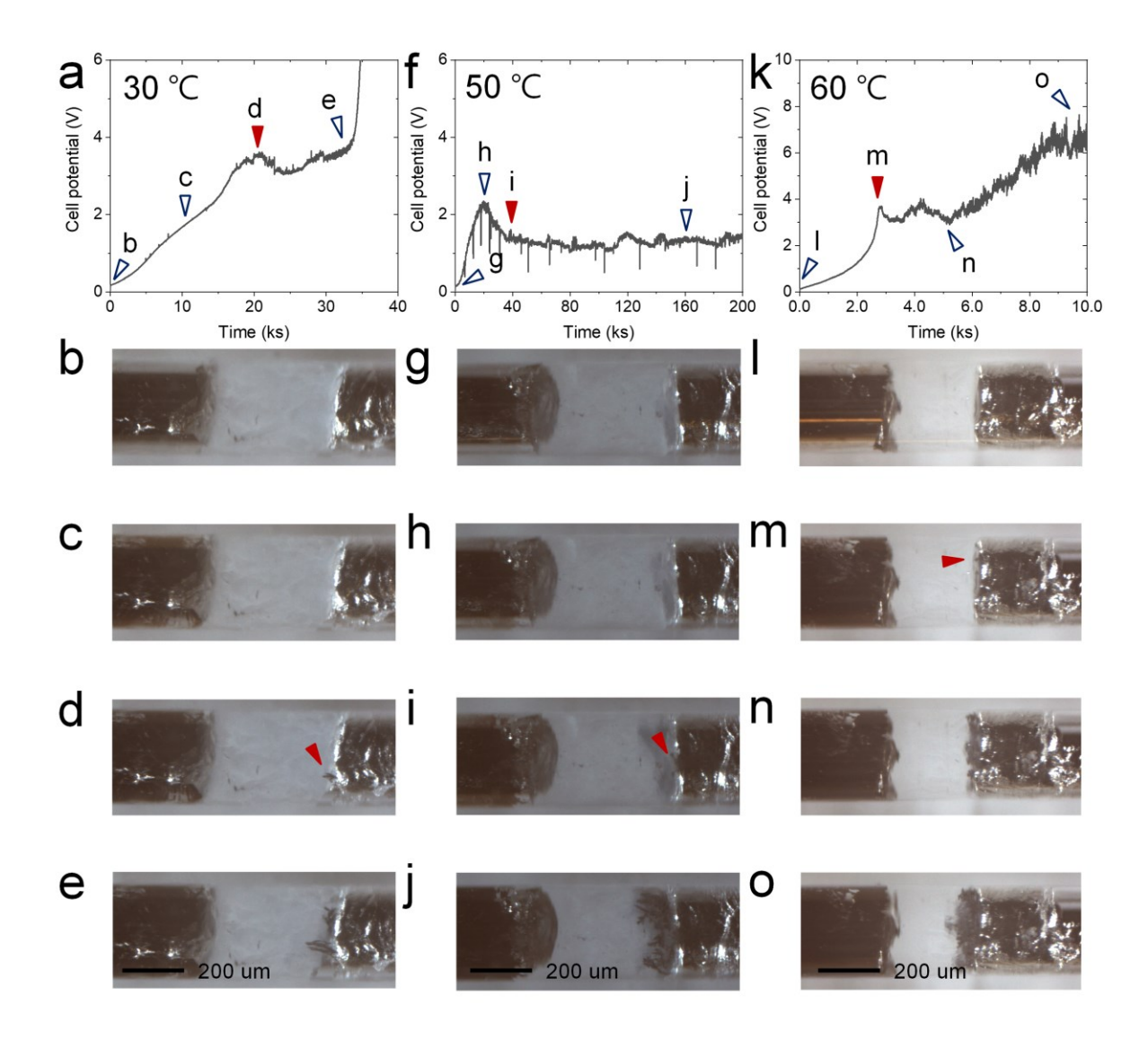


Fig. 3. Representative voltage curves and corresponding *operando* images of the glass capillary cells during galvanostatic charging. (a-e) 30 °C, current density of 0.03 mA / cm². (f-j) 50 °C, current density of 0.15 mA / cm². (k-o) 60 °C, 0.4 mA / cm². The points labeled by the red arrowheads mark the Sand's time.

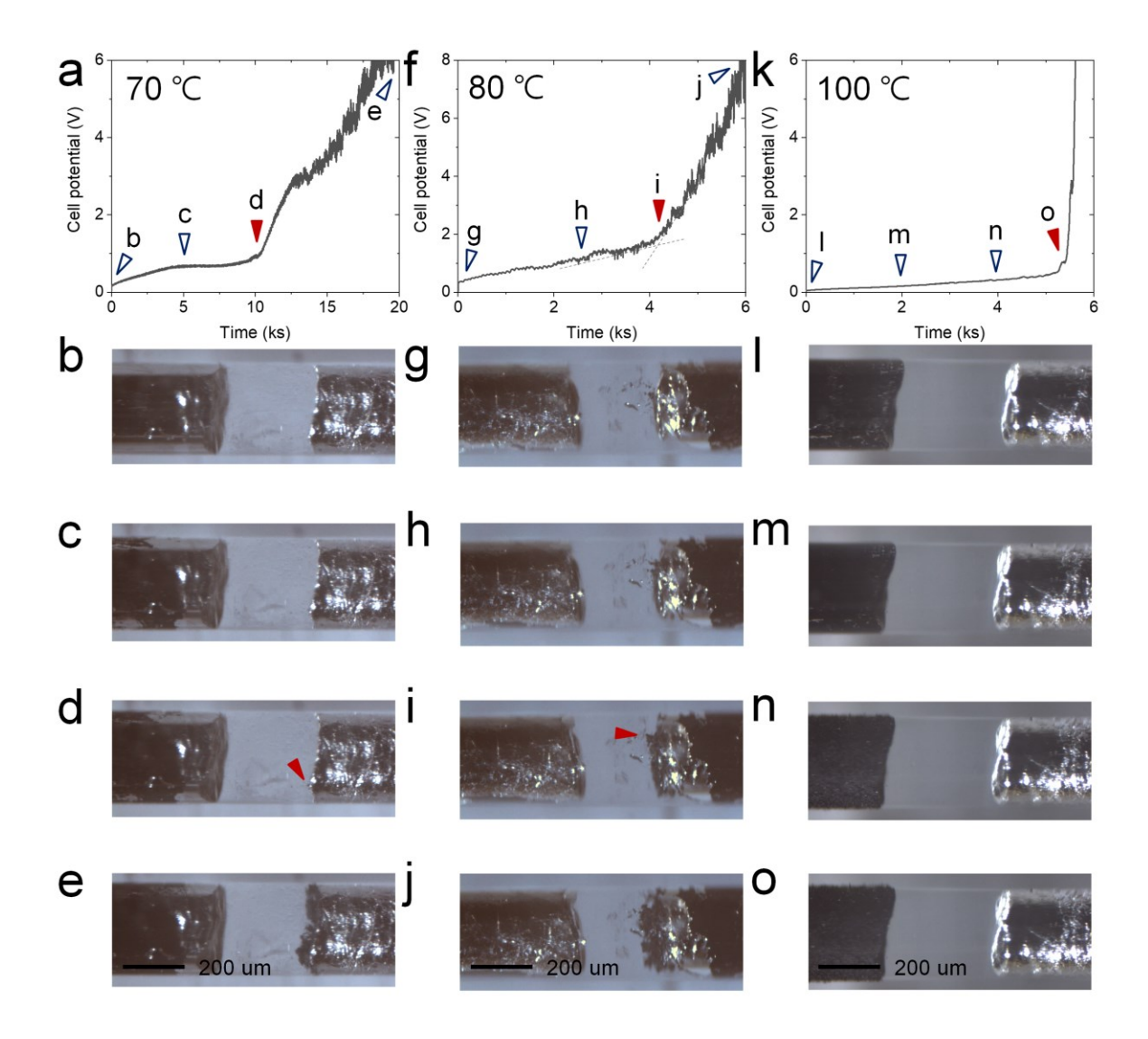


Fig. 4. Representative voltage curves and corresponding *operando* images of the glass capillary cells during galvanostatic charging. (a-e) 70 °C, current density of 0.03 mA / cm². (f-j) 80 °C, current density of 0.15 mA / cm². (k-o) 100 °C, 1.2 mA / cm². The points labeled by the red arrowheads mark the Sand's time.

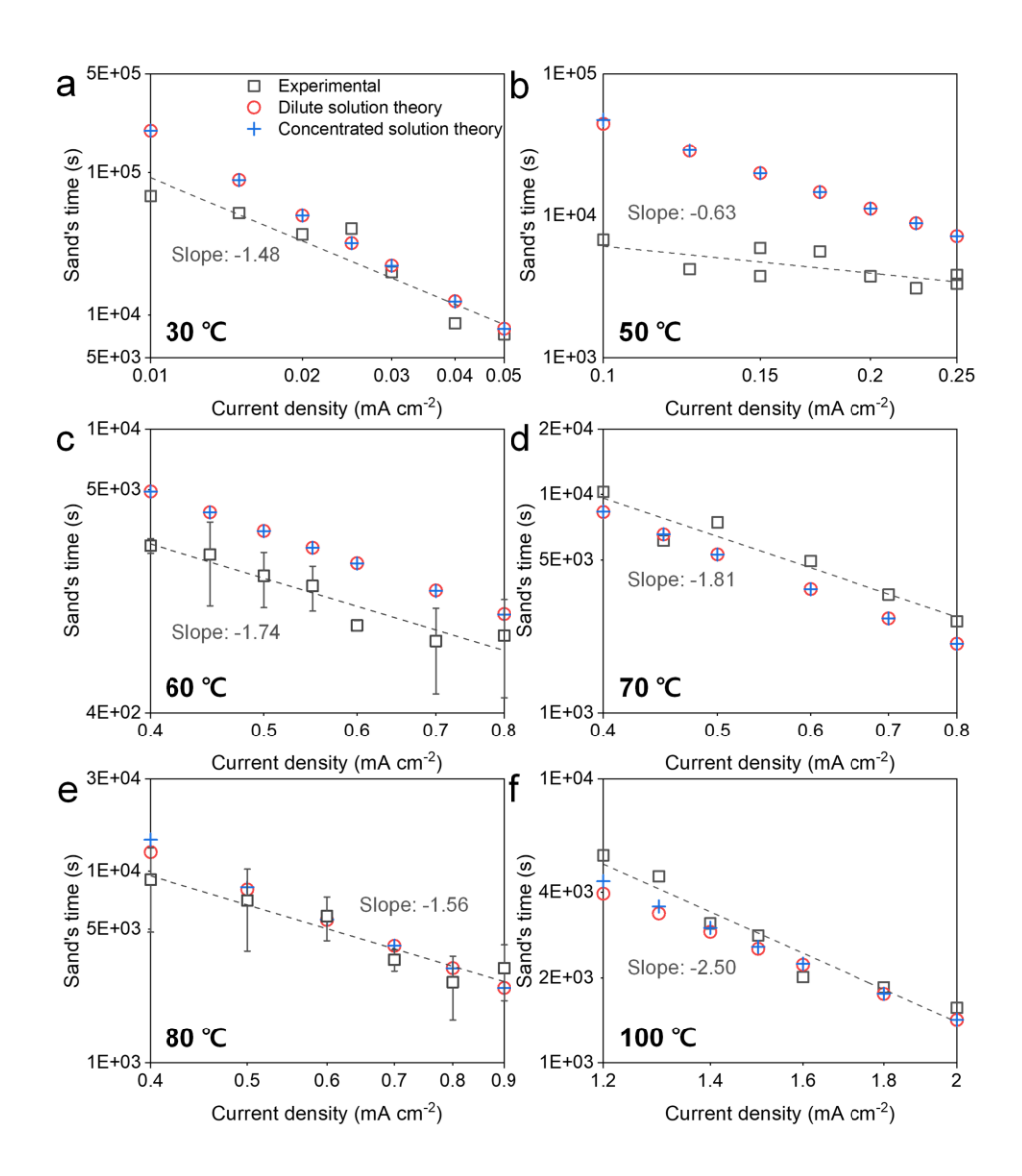


Fig. 5. Logarithmic plot of measured Sand's time versus the current density, compared with predictions from dilute and concentrated solution theory. For the concentrated solution theory model, a value of 2 was used for the thermodynamic factor $(1 + \partial \ln \gamma / \partial \ln m)$. For 60 °C and 80 °C data, average values were presented with error bars which show standard deviations.

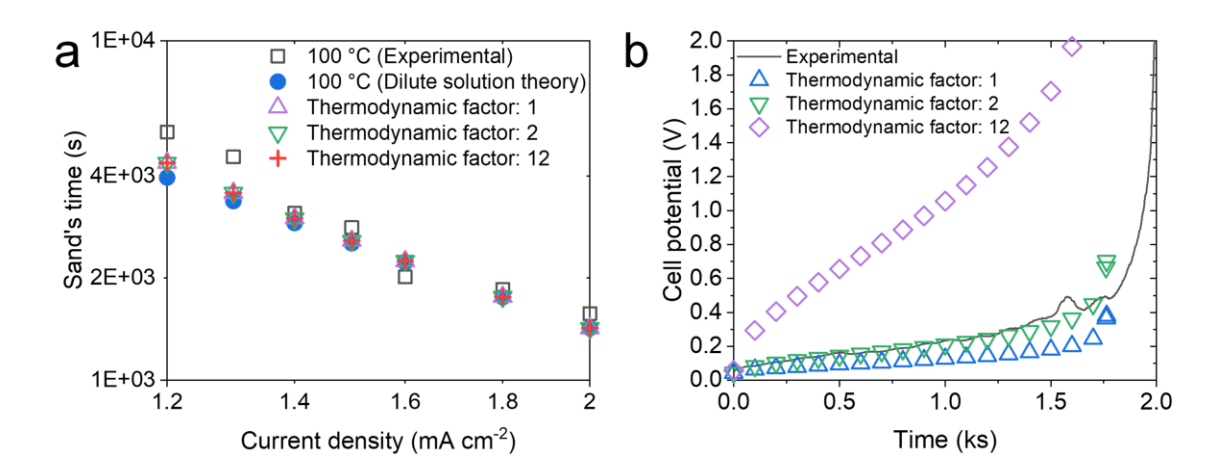


Fig. 6. (a) Sand's time and (b) example cell potential (100 °C, 1.8 mA / cm²), predicted by the concentration model with different thermodynamic factor $(1 + \partial \ln \gamma / \partial \ln m)$ values.